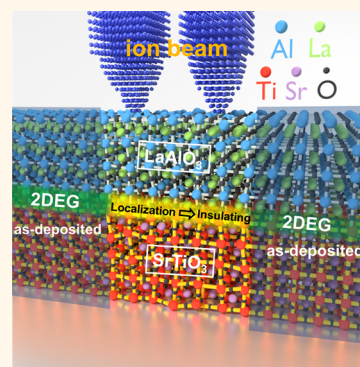


Tuning the Interface Conductivity of $\text{LaAlO}_3/\text{SrTiO}_3$ Using Ion Beams: Implications for Patterning

Sinu Mathew,^{†,‡,⊗} Anil Annadi,^{†,§,⊗} Taw Kuei Chan,^{§,⊥} Teguh Citra Asmara,^{†,§,||} Da Zhan,[#] Xiao Renshaw Wang,^{†,▽} Sara Azimi,^{§,⊥} Zexiang Shen,[#] Andriwo Rusydi,^{†,§,||} Ariando,^{†,§} Mark B. H. Breese,^{†,§,⊥,||} and T. Venkatesan^{†,‡,§,*}

[†]NUSNNI-NanoCore, National University of Singapore, Singapore 117411, [‡]Department of Electrical and Computer Engineering, National University of Singapore, Singapore, 117576, [§]Department of Physics, National University of Singapore, Singapore, 117542, [⊥]Center for Ion Beam Applications (CIBA), Department of Physics, National University of Singapore, Singapore 117542, ^{||}Singapore Synchrotron Light Source (SSLS), National University of Singapore, Singapore 117603, [#]Division of Physics and Applied Physics, School of Physical and Mathematical Sciences, Nanyang Technological University, Singapore 637371, and [▽]MESA+ Institute for Nanotechnology, University of Twente, Enschede 7500 AE, The Netherlands. [⊗]S. Mathew and A. Annadi contributed equally.

ABSTRACT Patterning of the two-dimensional electron gas formed at the interface of two band insulators such as $\text{LaAlO}_3/\text{SrTiO}_3$ is one of the key challenges in oxide electronics. The use of energetic ion beam exposure for engineering the interface conductivity has been investigated. We found that this method can be utilized to manipulate the conductivity at the $\text{LaAlO}_3/\text{SrTiO}_3$ interface by carrier localization, arising from the defects created by the ion beam exposure, eventually producing an insulating ground state. This process of ion-beam-induced defect creation results in structural changes in SrTiO_3 as revealed by the appearance of first-order polar TO_2 and TO_4 vibrational modes which are associated with Ti–O bonds in the Raman spectra of the irradiated samples. Furthermore, significant observation drawn from the magnetotransport measurements is that the irradiated (unirradiated) samples showed a negative (positive) magnetoresistance along with simultaneous emergence of first-order (only second order) Raman modes. In spectroscopic ellipsometry measurements, the optical conductivity features of the irradiated interface are broadened because of the localization effects, along with a decrease of spectral weight from 4.2 to 5.4 eV. These experiments allow us to conclude that the interface ground state (metallic/insulating) at the $\text{LaAlO}_3/\text{SrTiO}_3$ can be controlled by tailoring the defect structure of the SrTiO_3 with ion beam exposure. A resist-free, single-step direct patterning of a conducting $\text{LaAlO}_3/\text{SrTiO}_3$ interface has been demonstrated. Patterns with a spatial resolution of $5\ \mu\text{m}$ have been fabricated using a stencil mask, while nanometer scale patterns may be possible with direct focused ion beam writing.



KEYWORDS: heterointerface · ion irradiation · point defects · interface conductivity · localization · spectroscopic ellipsometry · interface patterning

The two-dimensional electron gas (2DEG) formed at the interface between two insulators LaAlO_3 (LAO) and SrTiO_3 (STO) is one of the most fascinating systems in the field of oxide electronics.¹ This interface 2DEG is shown to host novel phenomena such as superconductivity,² magnetism,^{3–6} tunable metal–insulator ground state,^{7,8} strong spin–orbit coupling,^{9,10} and crystallographic anisotropy.¹¹ Further, unconventional interfacial superconductivity along with magnetic order has been proposed in one-dimensional electron gas formed at this interface.¹² Room-temperature electronic devices,^{7,8} sensors, and nanophotodetectors^{13,14} have

been demonstrated in these interfaces. Very recently, scaling violation of fundamental Ohm's law have been reported in this material system when the 2DEG is confined to nano dimensions.¹⁵ The above device concepts have been realized by reducing the dimensionality of 2DEG at this interface. Lithography with multiple steps such as resist coating, beam exposure, hard mask of amorphous LaAlO_3 or AlO_x deposition and etching, or surface engineering of SrTiO_3 , combined with pulsed laser deposition (PLD) were utilized for patterning $\text{LaAlO}_3/\text{SrTiO}_3$.^{16–18} Nanostructures of interface 2DEG were also achieved by writing charges

* Address correspondence to venky@nus.edu.sg.

Received for review June 4, 2013 and accepted November 9, 2013.

Published online November 09, 2013
10.1021/nn4028135

© 2013 American Chemical Society

using conducting atomic force microscopy.⁸ However, in all these approaches either the presence of residual hard mask in the film along with the number of sophisticated process steps, or the stability of the pattern in ambient conditions is an issue of concern. Lithography along with reactive ion etching (RIE) has been used extensively to fabricate controlled structures of various materials. However, heavy ions present in the commonly used RIE plasma transforms insulating SrTiO₃ to a conductor.¹⁹ Thus, RIE cannot be applied in patterning oxide interfaces such as LaAlO₃/SrTiO₃. To achieve high quality devices and also to investigate the above-mentioned exotic phases from these unique interfaces, a reliable and simple patterning process is essential, but has not yet been realized. The important factor in patterning these conducting interfaces is to create a spatially insulating state. In this report, we demonstrate a novel way to create an insulating state and also to tailor the conductivity of the 2DEG at the LaAlO₃/SrTiO₃ interface using an ion beam exposure-based single-step strategy.

In recent years, ion beam exposure has emerged as a novel way to tailor the structural, mechanical, electronic, and even magnetic properties of materials by inducing atomic defects in a controlled manner.^{20–23} Recent experiments with ion/electron beam exposure to various nanomaterials and devices have proven to create beneficial effects in providing devices with desired functionalities,^{21,24,25} which has further found applications in nanoelectronics,^{20–25} energy,²¹ nanobiotechnology, *etc.*²⁶ Ion irradiation of oxide materials has been utilized for both device fabrication and material modification.^{21,27} In particular, energetic proton beams were found to be most useful for patterning and device fabrication.^{28,29} Very recently, coupled wave guides on a silicon-on-insulator platform have been fabricated by combining electrochemical etching with proton irradiation of a few tens of keV energy,³⁰ while low energy (less than 1 keV) ions were found to be useful in the patterning of complex magnetic nanoparticles to nanoscale dimensions.³¹ Significantly, in a recent report, Hong *et al.*³² reported the tunability of the electronic characteristics of ZnO field effect transistors by proton beam irradiation (few tens of MeV), which further enhanced the potential use of high energy proton irradiation for tailoring the material properties.

In this study, LaAlO₃/SrTiO₃(100) interfaces were exposed to a 2 MeV proton beam, and the electrical transport, vibrational and optical properties of the samples were investigated as a function of ion fluence. We found that the metallic behavior of the 2DEG changes significantly with proton beam exposure, at a fluence of 2×10^{17} ions·cm⁻² strong localization appeared in the 2DEG, and eventually at a fluence of 6×10^{17} ions·cm⁻² the interface became insulating. This process of metal to insulator transition occurs

through localization of mobile electrons *via* ion-induced defects, which results in structural changes in SrTiO₃ as revealed by Raman spectroscopy. Raman spectra showed the appearance of first-order modes of SrTiO₃, which indicate the presence of polar regions in the irradiated samples. Spectroscopic ellipsometry analysis of the ion exposed samples displays the appearance of increased scattering centers at the interface compared to the as-deposited case. The creation of a spatially selective insulating ground state by tuning the process parameters of an energetic ion beam-based single-step approach enable us to both pattern and also tune the electronic properties of the 2DEG.

RESULTS AND DISCUSSION

The LaAlO₃/SrTiO₃(100) samples were prepared by pulsed laser deposition by ablating a LaAlO₃ target onto TiO₂ terminated SrTiO₃(100) substrates. Samples were prepared in a range of oxygen pressure (PO₂) of $1–5 \times 10^{-3}$ Torr at 750 °C. Proton irradiation experiments and measurements were performed on the eight unit cells of LaAlO₃ on SrTiO₃ [(8 uc)LaAlO₃/SrTiO₃] sample deposited at PO₂ of 1×10^{-3} Torr. To make a systematic comparison, ion irradiation experiments were carried out as a function of ion fluence on a single LaAlO₃/SrTiO₃ sample (5×5 mm²) consisting of four identical sections (2×2 mm²) that are electrically isolated from each other (see Experimental Methods for details). Three out of the four sections of the same sample were exposed to proton beam, and the fourth region was kept unirradiated (defined as “as-deposited” in the following discussions). The ion fluences used were 1×10^{15} , 1×10^{16} , and 2×10^{17} ions·cm⁻², respectively. The details of the sample preparation are given in Supporting Information S1.

The electrical transport properties of the as-deposited and irradiated (8 uc)LaAlO₃/SrTiO₃ sections of the same sample were analyzed. The temperature dependence of the resistance $R(T)$ for the as-deposited and irradiated sections is shown in Figure 1a. The as-deposited section of the sample exhibits a typical metallic behavior similar to the conventional LaAlO₃/SrTiO₃ interfaces at this 8 uc LaAlO₃ thickness,^{33–35} whereas for the irradiated sections, a gradual change in the resistance at 300 K is observed with ion fluence. As the proton fluence is increased, clear localization behavior in transport starts to emerge at low temperatures with the signature of increase in base resistance at 2 K. The resistance of the sample section irradiated with 2×10^{17} ions·cm⁻² became 0.1 MΩ at 2 K and the resistance minimum in the $R(T)$ curve is found to shift towards higher temperature with an increase in ion fluence. The above $R(T)$ behavior gives adequate indication that ion exposure effects have created a high resistive state for the 2DEG through localization of the mobile electrons. The drastic upturns

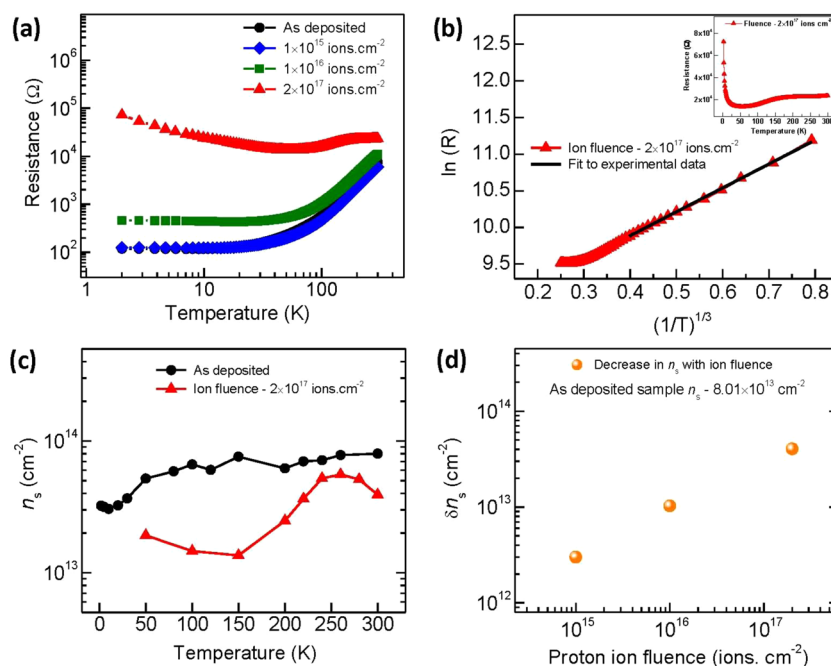


Figure 1. Electrical transport data of as-deposited and 2 MeV proton-beam-exposed (8 uc)LaAlO₃/SrTiO₃ sample sections. (a) Temperature-dependent resistance of as-deposited and ion beam exposed sample sections at different proton fluences. (b) Variable range hopping fit to transport data of ion irradiated with 2×10^{17} ions \cdot cm⁻² fluence; inset shows the nonsaturating behavior of the corresponding sample section. (c) Temperature dependence of carrier density (n_s) of as-deposited and ion-irradiated sample at a fluence of 2×10^{17} ions \cdot cm⁻². (d) Reduction in carrier density δn_s with ion fluence at 300 K; here δn_s is defined as the difference in n_s of as-deposited and irradiated sample sections ($\delta n_s = n_{s(\text{as-deposited})} - n_{s(\text{irradiated})}$).

in resistance toward low temperatures would be expected in transport mechanisms such as variable range hopping (VRH) in a strong localization regime or a magnetic Kondo scattering, which operates at this interface.^{3,35} The $R(T)$ curve for the case of 2×10^{17} ions \cdot cm⁻² does not show any saturation even up to 2 K (inset of Figure 1b) inferring that Kondo scattering may not be the governing mechanism. The low temperature resistance behavior is further analyzed to the VRH mechanism: in the VRH regime R follows a $(1/T)^{1/n+1}$ (n = dimensionality of the system) dependence. A VRH fitting (with $n = 2$) of the experimental data for a fluence of 2×10^{17} ions \cdot cm⁻² case is shown in Figure 2b, and a clear $(1/T)^{1/3}$ dependence is observed below 30 K. The 2D nature of the VRH mechanism is further confirmed using a self-consistent analysis (Supporting Information S2). The hopping radius is estimated (Supporting Information S2) to be about 14–30 nm, which is relatively larger than the typical dimensionality (5–10 nm) of the 2DEG. Thus, the hopping mechanism must be most likely 2D in nature.

The other important quantity that can give further insight to the localization behavior is the carrier density (n_s). The n_s for as-deposited and each irradiated section of (8 uc)LaAlO₃/SrTiO₃ sample were extracted from Hall effect measurements. Figure 1c shows the temperature dependence of the n_s for the as-deposited and irradiated at a fluence of 2×10^{17} ions \cdot cm⁻². The n_s for the as-deposited section of the sample is about 8×10^{13} cm⁻² at 300 K. In comparison, the irradiated

section shows a significant decrease in n_s with about 4×10^{13} cm⁻² at 300 K. The as-deposited and irradiated samples show similar temperature dependence of carrier density. The percentage change in both cases is of the same order. However, in the irradiated case the defects created can trap the charges and decrease the effective mobile electrons and enhance the localization. Figure 1d shows the decrease in carrier density (δn_s) with proton fluence at 300 K. Here δn_s is defined as the difference in the n_s of as-deposited and n_s of irradiated sections ($\delta n_s = n_{s(\text{as-deposited})} - n_{s(\text{irradiated})}$). From Figure 1d it is clear that δn_s increases with the proton fluence, and at fluence of 2×10^{17} ions \cdot cm⁻² δn_s became 4×10^{13} cm⁻². The above data clearly indicate that the proton beam exposure with a fluence of 2×10^{17} ions \cdot cm⁻² can reduce as many as 3–4 $\times 10^{13}$ cm⁻² mobile carriers of the 2DEG at the interface, which is most possibly accomplished by localization of carriers within the lattice of SrTiO₃. From the above conclusion one can expect that the interface samples having initial $n_s \leq 4 \times 10^{13}$ cm⁻² become insulating at these ion fluences because of the complete localization of carriers. In order to validate this possibility, a conducting LaAlO₃/SrTiO₃ sample having an initial carrier density of 1.9×10^{13} cm⁻² (achieved by controlling the oxygen pressure during the growth) has turned to become insulating with the exposure of proton beam at a fluence of 2×10^{17} ions \cdot cm⁻² (see Supporting Information S3). A table showing the decrease of carrier density with ion irradiation on various samples is given in Supporting Information S1.

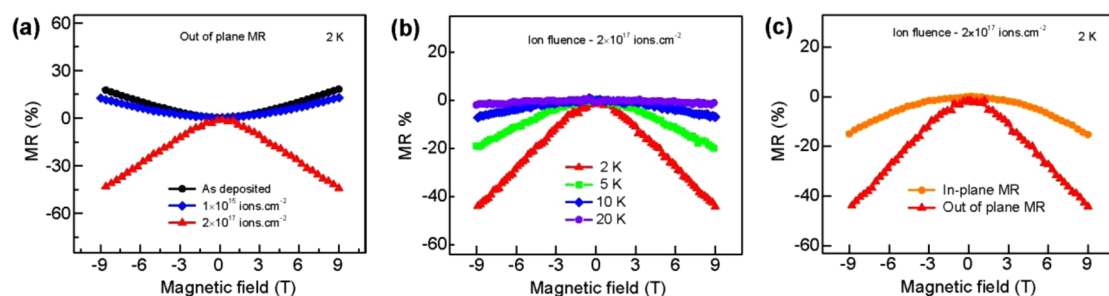


Figure 2. Magnetoresistance (MR) of the (8 uc)LaAlO₃/SrTiO₃ sample sections with different proton fluences: (a) out of plane MR at 2 K, (b) out of plane MR at 2, 5, 10, and 20 K, and (c) in-plane and out of plane MR for the sample section irradiated with 2×10^{17} ions·cm⁻².

To evaluate the localized transport behavior at low temperature in the above ion exposed samples, a detailed magnetoresistance (MR) study was carried out. MR is a useful tool to investigate the transport mechanisms such as localization and magnetic scattering. MR measurements were performed in in-plane and out of plane modes. Figure 2a shows the out of plane MR (magnetic field H perpendicular to the interface) measured for different ion fluences and as-deposited sections at 2 K with H up to 9 T. Both as-deposited and low fluence (1×10^{15} ions·cm⁻²) sections display a positive MR behavior. The positive MR is a characteristic of orbital scattering in the presence of a magnetic field due to the change in electron transit paths. On the other hand the section exposed with 2×10^{17} ions·cm⁻² fluence shows a negative MR behavior. Comparison of the MR with respect to ion fluence infers that the MR slowly changes sign from positive to negative with increasing ion fluence. The large negative and nonsaturating MR observed in the irradiated case is an additional indication of the localization behavior discussed earlier (in Figure 1). The electron transport in the strongly localized regime can exhibit a negative MR, which is a consequence of the magnetic field disrupting the self-interference of the electrons undergoing localization. The temperature dependence of the out of plane MR measured for a fluence of 2×10^{17} ions·cm⁻² is shown in Figure 2b. The magnitude of MR gradually decreases with increase in temperature, which can be understood as the effect of enhanced thermal fluctuations in the scattering process. Figure 2c shows the comparison of in-plane (H applied parallel to the interface) and out of plane MR for the 2×10^{17} ions·cm⁻² case where both display a negative MR, however with a difference in MR magnitude. The orbital scattering is excluded in this in-plane geometry due to the absence of Lorentz forces on carriers. This MR dependence is consistent with the previous reports.³⁵

The detailed electron transport and MR analysis discussed above clearly indicates a dependence on ion fluence for carrier localization and point towards the possibility of creating insulating regions in 2DEG. It is known that the 2DEG is accumulated on the Ti

orbitals of SrTiO₃ for LaAlO₃/SrTiO₃ interfaces.³⁶ Since the ion irradiation produces dramatic changes in the transport of the 2DEG that resides in SrTiO₃, it is necessary to understand the effects of ion irradiation on SrTiO₃. Recent reports on SrTiO₃-based interfaces reveal that an atomic distortion of the SrTiO₃ lattice and defects in SrTiO₃ at the interface can manipulate the transport properties of 2DEG significantly.^{37–41} The ion beam exposure process is expected to influence the structural and electronic properties of the material by inducing atomic defects. In order to investigate the ion irradiation effects on structural and electronic properties of the LaAlO₃/SrTiO₃ samples, Raman spectroscopy and spectroscopic ellipsometry experiments were carried out.

The nature of the induced defects and resultant possible microscopic structural changes in LaAlO₃/SrTiO₃ samples due to ion irradiation can be gained using Raman spectroscopy, which was performed on as-deposited and irradiated sections of the sample. The probing depth of Raman scattering signal was 2 μ m from the top surface of the sample. Since the thickness of LaAlO₃ is 8 uc (3.2 nm) and also the interference enhancement of the Raman signal is negligible in this system, the Raman spectrum of the sample is dominated by the modes from the substrate SrTiO₃. SrTiO₃ at room temperature has an ideal cubic perovskite structure with a space group $Pm\bar{3}m (O_h^1)$.⁴² There are five atoms per unit cell, each of which is located at a point of inversion symmetry. The optical phonons in the cubic phase are of odd parity, which accounts for the absence of first-order Raman scattering in SrTiO₃ single crystals.^{43–45} Even though the first-order modes are Raman inactive, SrTiO₃ shows a Raman spectrum with broad peaks that arise from higher-order modes which involve the creation or destruction of two or more first-order modes. Raman spectra for the irradiated and as-deposited sections of the sample are shown in Figure 3. As expected, the spectra are dominated by SrTiO₃ modes. In the spectrum of the as-deposited case, broad second-order peaks are clearly visible at 75, 200–500, and 600–800 cm⁻¹. Significantly, for the ion beam exposed portions, additional peaks emerge at 175, 540, and 795 cm⁻¹ along with

increasing fluence (additional peak positions are indicated with dotted lines). These peaks are identified as symmetry-forbidden first-order modes arising from transverse optic TO_2 , TO_4 , and longitudinal optic LO_1 , LO_4 phonons as indicated in Figure 3.^{46–48} The appearance of first-order modes in the irradiated sections of the sample clearly indicates a lowering of crystal symmetry for the $SrTiO_3$ and thus the loss of the inversion center.^{46–48} First-order Raman scattering has been observed in thin films, nanostructures of $SrTiO_3$, and also single crystals with lifted center-of-symmetry by the application of an external electric field.^{46–49} The line shape of the TO_2 peak is strongly asymmetric; *i.e.*, the scattering intensity increases at the high-energy side and is depressed at the low-energy side of the peak and displays a Fano profile. The Fano effect occurs whenever discrete excitations and a broad continuum interfere coherently.^{46–48} We speculate that the ion damaged regions in $SrTiO_3$ result

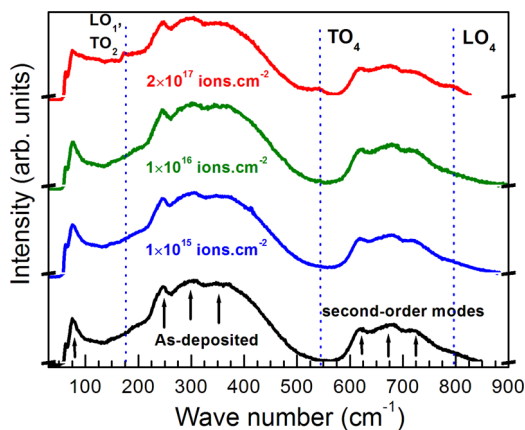


Figure 3. Raman spectra of as-deposited and proton-beam-exposed sample sections of (8 uc)LaAlO₃/SrTiO₃.

in a polar material with a continuum that interacts with the polar TO phonons. Such asymmetric line shapes have been observed for polar TO_2 modes in $SrTiO_3$ thin films and have been ascribed to the interaction of the phonon with a continuum arising from rapid polarization fluctuations.^{46–48} Although TO_4 is also a polar phonon, its energy is much higher, the density of states for continuum most likely vanishes at this frequency, and thus, Fano asymmetry has not been observed in the case TO_4 mode.⁴⁷ The origin of the TO_2 and TO_4 modes is associated with Ti–O bonding in the $SrTiO_3$.^{46–48} In our recent report on LaAlO₃/SrTiO₃(110) interfaces it is shown that the electron transport of the 2DEG is highly anisotropic,¹¹ and it is critically linked to the Ti–O crystallographic arrangement, which further emphasizes the significance of this Ti–O bonding. Raman spectra analysis of an irradiated bare STO substrate has also shown the appearance of first-order modes, which supports the above discussion (Supporting Information S4).

To further understand the effects of the irradiation on the electronic band structure of the LaAlO₃/SrTiO₃ interface, spectroscopic ellipsometry measurements were performed on pristine and ion exposed (fluence of 2×10^{17} ions·cm⁻²) portions of the substrate SrTiO₃ and 8 uc LaAlO₃/SrTiO₃ sample. Figure 4a,b shows the complex dielectric function $\epsilon(\omega) = \epsilon_1(\omega) + i\epsilon_2(\omega)$ of the samples as extracted from the ellipsometry data as a function of incident photon energy ω . The details of the data analysis is given in Supporting Information S5. From Figure 4b, it can be seen that the ϵ_2 spectra of both SrTiO₃ and the LaAlO₃/SrTiO₃ interface have two main peaks centered at 4.2 and 5.0 eV, respectively. These two peaks are assigned to the optical transition from O-2p state (the valence band) to Ti-3d- t_{2g} state (the conduction band).^{50–52} The peak at 4.2 eV arises

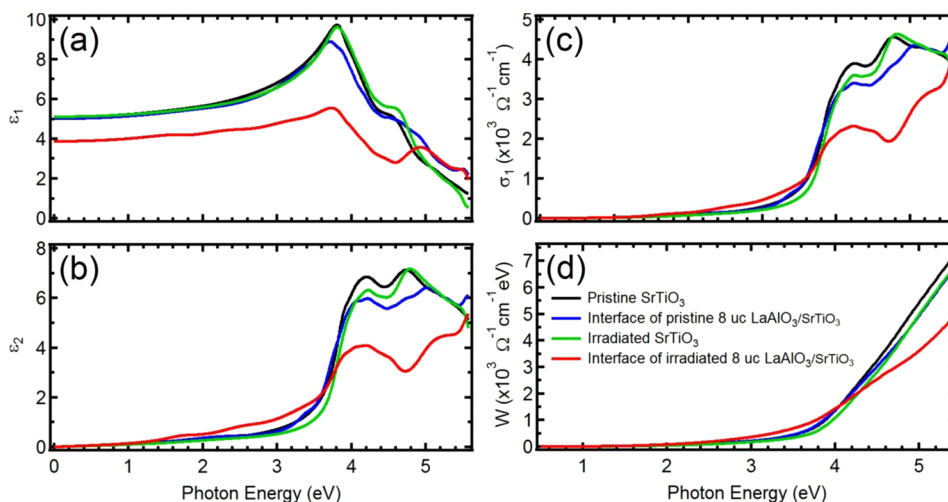


Figure 4. Complex dielectric function, optical conductivity, and spectral weight of pristine SrTiO₃, irradiated SrTiO₃, pristine (8 uc)LaAlO₃/SrTiO₃ and irradiated (8 uc)LaAlO₃/SrTiO₃ as extracted from the spectroscopic ellipsometry data. The irradiated sample mentioned above corresponds to 2 MeV protons at a fluence of 2×10^{17} ions·cm⁻². (a) Real part of dielectric function ϵ_1 . (b) Imaginary part of dielectric function ϵ_2 . (c) Optical conductivity σ_1 . (d) Spectral weight W .

from the transition at the center of the Brillouin zone (Γ -point) of SrTiO₃, while the peak at 5.0 eV is due to the transition at the M-point of SrTiO₃. Thus, by analyzing the differences of $\varepsilon(\omega)$ between the as-deposited and irradiated portions, one can study the effect of ion beam exposure on the band structure around the O-2p and Ti-3d- t_{2g} states of LaAlO₃/SrTiO₃. From Figure 4a,b the $\varepsilon(\omega)$ of irradiated LaAlO₃/SrTiO₃ portion changes dramatically in comparison with the bare STO and as-deposited LaAlO₃/SrTiO₃ portion. For ε_2 , the overall shape of the features between 0.5–5.4 eV is broadened; ε_2 decreases between 3.6–5.4 eV (*i.e.*, around the two peak centers), while it increases below 3.6 eV (*i.e.*, the peak tail region). According to the Drude–Lorentz model of the dielectric function used to fit the ellipsometry data (Supporting Information S5), the peak line width is controlled by the scattering rate parameter $\Gamma_k \sim 1/\tau$, where τ is the electron relaxation time. In this case, the peak broadening suggests an increase of Γ_k and correspondingly a decrease in τ . The decrease of τ indicates that the irradiated interface contains more scattering centers that can impede the motion of the electrons and thus point toward the presence of increased localization effects at the interface. Another important point is the fact that the M-point peak shifts into higher energy, from 5 to 5.3 eV from ε_2 plot in (b), which means that the irradiation also changes the band structure by further separating the valence band and the conduction band at the M-point. We have analyzed the second derivatives of $\varepsilon(\omega)$ to identify the van Hove singularities of the LaAlO₃/SrTiO₃ interface and thus distinguish the various optical interband transitions from the highest valence bands to the lowest conduction bands at various regions in the Brillouin zone.⁵³ The above analysis given in the Supporting Information S5 also supports this observation of the shift of the M point to higher energy. Furthermore, the overall intensity ε_1 of the irradiated LaAlO₃/SrTiO₃ interface is also found to be decreased compared to that of as-deposited LaAlO₃/SrTiO₃ interface.

The optical conductivity $\sigma_1(\omega) = \varepsilon_0 \varepsilon_2(\omega) \omega$ of the samples were calculated from the $\varepsilon(\omega)$ data and is shown in Figure 4c. The analysis of σ_1 is linked to the effective number of electrons excited by the photon, n_{eff} , via the f-sum rule⁵⁴

$$\int_0^{\infty} \sigma_1(\omega) d\omega = \frac{he^2}{4mV} n_{\text{eff}} \quad (1)$$

where e is the elementary charge, m is the electron mass, and V is the volume of the unit cell. Thus, by integrating σ_1 over a particular energy range (in this case 0.5–5.4 eV) the partial spectral weight W can be obtained, which is related to the total number of electrons being excited in that particular energy range. Figure 4d shows the W of each sample. From the plots it can be seen that the spectral weight at 5.4 eV (*i.e.*, the

measurement limit) of the irradiated LaAlO₃/SrTiO₃ interface is much less than the as-deposited LaAlO₃/SrTiO₃ interface. A more detailed quantitative analysis of W (Supporting Information S5) reveals that the number of charges related to the 5 eV transition in the irradiated LaAlO₃/SrTiO₃ interface is decreased by as much as $\sim 0.4e$. However, it should be noted that this decrease may also be due to charge transfer into higher energy regions, which requires high-energy optical spectroscopy data.⁵⁵

The conductivity of the same LaAlO₃/SrTiO₃ sample measured before and after irradiation showed an increase in 2DEG resistance with fluence. In a separate experiment, a SrTiO₃ substrate irradiated with a fluence of 2×10^{17} ions \cdot cm⁻² did not show any change in the insulating nature of the SrTiO₃ within the sensitivity of our measurements (10^8 ohms). This confirms that the current irradiation experiments do not simply create oxygen vacancies alone, but also generate compensating cationic vacancies, and at higher fluences other defect complexes that can trap charges efficiently. This is a benefit as the low Z ion beam will not produce a parallel conducting path in the SrTiO₃ as in the cases with low energy heavy ion irradiations.¹⁹

To explore the patterning capability of the interface using ion beam exposure technique, a sample of (8 uc)LaAlO₃/SrTiO₃ was grown under identical conditions and selectively exposed with 2 MeV protons in two regions (500 μ m width and 2 mm in length) at fluences of 2×10^{17} and 6×10^{17} ions \cdot cm⁻². Thus we have a (8 uc)LaAlO₃/SrTiO₃ sample encompassing two ion-irradiated rectangular sections with a pristine portion as shown in Figure 5a. Raman spectroscopy and imaging and electrical transport measurements were carried out on this sample. As shown in the Figure 5b the Raman spectrum displays similar behavior as in the previous case. The intensity of the polar modes was found to increase with ion fluence and is strongly reflected in the observation of a stronger intensity profile for the polar mode peaks in the spectrum. Furthermore, a Raman spectroscopy image produced using the integrated intensity of TO₄ mode at 540 cm⁻¹ of the irradiated sample is shown in Figure 5c. The as-deposited and the irradiated regions at a fluence of 2×10^{17} and 6×10^{17} ions \cdot cm⁻² are clearly distinguishable in the intensity profile. Here for the as-deposited section (with an electrically conducting state, Figure 5d) the signal from the TO₄ mode is absent. However, the patterned line with 2×10^{17} ions \cdot cm⁻² (exhibiting strong localization, Figure 5(e)) shows a significant intensity of the TO₄ mode, indicating the emergence of structural changes in SrTiO₃ at this fluence. The highest intensity of the TO₄ mode is observed for the 6×10^{17} ions \cdot cm⁻² irradiated part and which is found to be electrically insulating. Raman imaging thus allows an indirect mapping of the interface conductivity of the ion-beam patterned LaAlO₃/SrTiO₃ system.

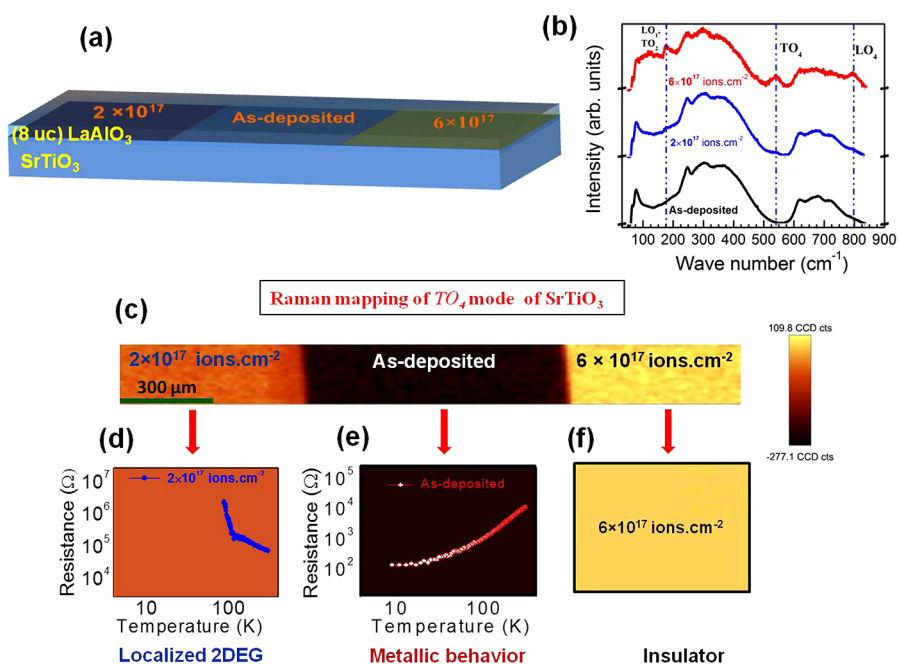


Figure 5. (a) A schematic representation of the ion-irradiated sample: lines having width 500 μm and length 2 mm made with different proton fluences on a (8 uc)LaAlO₃/SrTiO₃ sample. (b) Raman spectra obtained from the as-deposited and ion-beam-exposed at fluences of 2×10^{17} and 6×10^{17} ions · cm⁻² in the rectangular sample regions. (c) Raman image created from the integrated intensity of the TO₄ mode at 540 cm⁻¹ for as-deposited as well as patterned lines of LaAlO₃/SrTiO₃ sample sections. Temperature-dependent resistance of the corresponding patterned lines with (d) 2×10^{17} ions · cm⁻² (strong localization), (e) as-deposited (metallic behavior), and (f) 6×10^{17} ions · cm⁻² (insulator).

This clearly indicates the potential of this method to fabricate insulating regions in conducting LaAlO₃/SrTiO₃ samples. In addition, this also reveals the ability to tune the conductivity by simply adjusting the ion fluence.

An estimate of the defects created by the proton beam can be determined from Monte Carlo simulations (SRIM 2008)⁵⁶ using full damage cascade. Oxygen ions being the lightest in the SrTiO₃ lattice have maximum displacements compared to Ti and Sr under irradiation by energetic ions. If oxygen vacancies were the dominant defects in the MeV proton irradiated SrTiO₃, one would expect a reduction in resistance for the irradiated SrTiO₃ as observed by Kan *et al.*¹⁹ The displacement per atom (dpa) for Sr and Ti is found to be half that of oxygen.⁵⁶ The oxidation states of O, Ti, and Sr in SrTiO₃ are -2, +4, and +2, respectively. Thus the cationic and anionic vacancies will have different charges. The ion range of the 2 MeV proton in (8 uc)LaAlO₃/SrTiO₃ sample is about 27 μm. The oxygen vacancies estimated at the surface is $\sim 10^{20}$ cm⁻³ and at the end of range it is about $\sim 10^{21}$ cm⁻³ at an ion fluence of 6×10^{17} ions · cm⁻². The sputtering yield of oxygen at the LaAlO₃ surface is 10⁻⁴ atoms/ion, which gives the fraction of oxygen atoms sputtered from the LAO surface is less than 0.2% at a fluence of 6×10^{17} ions · cm⁻². For SRIM simulations sample is treated as an amorphous matrix with homogeneous mass density, and the ion kinetic energy is transferred ballistically to the target atom. The above calculated values are an overestimate because the crystalline nature (ion

channeling) and the annealing of the defects have not been incorporated in this simulation.²¹

To investigate the elemental redistribution across the interface and probe the crystalline quality of the irradiated LaAlO₃/SrTiO₃ sample, we have performed high resolution Rutherford back scattering (HRRBS) on as-deposited and irradiated sample at a fluence of 6×10^{17} ions · cm⁻² (details are given in Supporting Information S6). The analysis of HRRBS indicates that the irradiation effects on La redistribution and the variations in stoichiometry were very small and beyond the detection limit of HRRBS, which is about 4 Å. X-ray diffraction measurements (data not given here) on the above samples had shown broadening of SrTiO₃(200) peak, and the LaAlO₃(100) and (200) peaks were clearly visible in the spectra. Estimating the microscopic structural perturbations of the LaAlO₃ layer (top 3.2 nm in our samples) require techniques such as extended X-ray absorption fine structure (EXAFS).

Furthermore, to show the patterning capability for device applications, ion irradiation was carried out with the optimized parameters (fluence of 6×10^{17} ions · cm⁻² for 2 MeV protons) on a LaAlO₃/SrTiO₃ sample covered by a stencil mask, which is thick enough to stop the ion beam to create spatially selective insulating regions at the interface 2DEG. Figure 6a shows a scanning electron microscopy (SEM) image of the patterned LaAlO₃/SrTiO₃ sample using a metal stencil mask (made from 0.5 mm thick brass) with a Hall bar geometry (channel width ~ 150 μm). The Hall bar

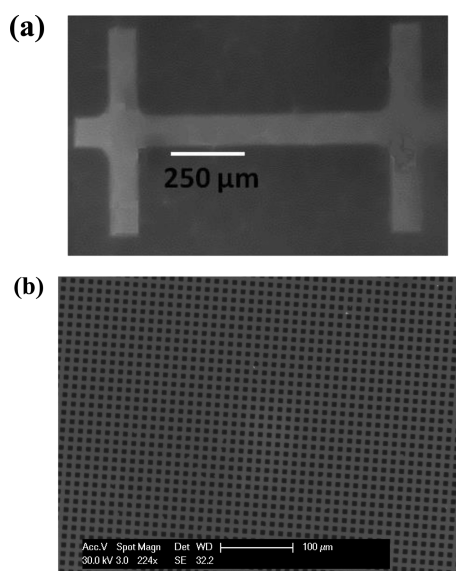


Figure 6. (a) Scanning electron microscopy (SEM) images of the patterned $\text{LaAlO}_3/\text{SrTiO}_3$ sample using (a) 2 MeV proton beams at a fluence of $6 \times 10^{17} \text{ ions} \cdot \text{cm}^{-2}$ with a hard mask of Hall bar geometry, (b) 500 keV helium ions at a fluence of $1 \times 10^{16} \text{ ions} \cdot \text{cm}^{-2}$ with a mask (made of gold) of size $5 \mu\text{m}$.

structure is found to be transferred to the sample with the expected dimensions. Significantly, the SEM image shows the contrast between the irradiated and as-deposited sections. The contrast for the secondary electrons at the conducting (as deposited) and insulating (irradiated) regimes is due to the difference in the number of secondary electrons reaching the Everhart–Thornley detector used in the SEM. We have also explored low energy helium ion irradiations (500 keV He) to create localization and insulating state in conducting $\text{LaAlO}_3/\text{SrTiO}_3$ interfaces as discussed earlier. An insulating state is found to be created at a fluence of $1 \times 10^{16} \text{ ions} \cdot \text{cm}^{-2}$ and strong localization at $1 \times 10^{15} \text{ ions} \cdot \text{cm}^{-2}$ in the case of helium ions (Supporting

Information S7). A pattern was formed using a mask made of gold with 500 keV helium ion irradiation, and the corresponding image is shown in Figure 6b. Here, the $5 \mu\text{m}$ conducting regions (the bright contrast), which are clearly visible in SEM micrographs, demonstrate the capability to pattern the interface down to lower dimensions. With the development of helium ion microscope with focused ion beams having spatial resolutions of sub-0.5 nm, direct patterning of fine conducting lines may be possible on the nm scale. This demonstrates the ability to pattern the $\text{LaAlO}_3/\text{SrTiO}_3$ interfaces using low Z-ions without any intermediate deposition or etching techniques that were previously employed.

CONCLUSIONS

A resist-free, single-step direct patterning of the conducting oxide interface in $\text{LaAlO}_3/\text{SrTiO}_3$ utilizing energetic ion beam exposure has been demonstrated. It is shown that this method is tunable to engineer the conductivity of the two-dimensional electron gas at the $\text{LaAlO}_3/\text{SrTiO}_3$ interface by inducing localizations *via* defects, as evidenced by electrical transport, Raman spectroscopy, and spectroscopic ellipsometric measurements. The spectroscopic studies reveal that the induced defects/distortions in the SrTiO_3 lattice can significantly manipulate the electrical ground state of the 2DEG in these systems. The further practical advantage of such low Z ion beam exposure is the elimination of undesired ion-beam-induced substrate conductivity (as seen with Ar ions), thus allowing us to custom-tailor the 2DEG formed at the oxide interface. Considering the limits of conventional lithography to pattern these interfaces due to the buried nature of the 2DEG, this new strategy may open up a novel way to pattern the conducting oxide interfaces whose properties are sensitive to the metal–oxygen bonds and the local crystal structure.

EXPERIMENTAL METHODS

Sample Preparation and Electrical Characterization. Ion irradiation was carried out using a 3.5 MV Singletron accelerator at the Center for Ion Beam Applications at the National University of Singapore. A collimated ion beam was used to raster-scan under normal incidence with a current density of $50 \text{ nA}/\text{mm}^2$ for protons and $10 \text{ nA}/\text{mm}^2$ for Helium ions. The pressure in the chamber during the irradiation was $1 \times 10^{-6} \text{ mbar}$. To produce a sample with four isolated equal sections, cross lines were made on the square SrTiO_3 substrate surface with a diamond cutter. Then, a LaAlO_3 film of 8 μm was deposited on to the partitioned SrTiO_3 substrate. Each section of the deposited $\text{LaAlO}_3/\text{SrTiO}_3$ sample had shown a conducting behavior, and the absence of conductivity between any two sections indicates good electrical isolation. The details of the sample preparation are given in Supporting Information S1. The electrical connections to the interface were made by Al wire bonding to the interface. The Al wire penetrates into the sample from the top surface and makes the connection across the interface that enables us to probe the $\text{LaAlO}_3/\text{SrTiO}_3$ interface conductivity. Hall measurements were performed to extract the carrier

density in these samples with $\pm 1.5 \text{ T}$, and the results fit well to a single carrier model in this low field regime.

Raman Spectroscopy. Visible Raman spectroscopy was carried out at room temperature using Renishaw Invia Raman system. The excitation wavelength used was 532 nm, and the laser power at the sample was below $1.0 \text{ mW}/\text{cm}^2$ to avoid any laser-induced damage. A $50\times$ objective lens was used with a laser spot size of $\sim 1 \mu\text{m}$, and the scattered light from the sample was collected in the back scattering geometry. Raman imaging was carried out using WITec ALPHA300RAS system using 532 nm excitation wavelength with a motorized stage.

Spectroscopic Ellipsometry. The spectroscopic ellipsometry measurements were performed in the spectral range between 0.5 and 5.4 eV by using a Sentech SE 850 ellipsometer at room temperature. The incident angle was set at 70° from the sample normal, and the incident light was linearly polarized and 45° from the plane of incidence. Specially designed lenses were used to focus the incoming light to achieve a beam spot size of $\sim 500 \mu\text{m}$. The analysis method to extract the complex dielectric function of the materials from the raw spectroscopic ellipsometry data is explained in the Supporting Information S5.

SEM. A scanning electron microscope (Philips XL30, FEG) was used to image the ion beam exposed LaAlO₃/SrTiO₃ samples. The beam energy used for the imaging was 30 keV with the sample normal to the scanning beam.

Conflict of Interest: The authors declare no competing financial interest.

Acknowledgment. We thank the National Research Foundation (NRF), Singapore, under the Competitive Research Program (CRP) "Tailoring Oxide Electronics by Atomic Control" NRF2008NRF-CRP002-024, National University of Singapore (NUS) cross-faculty grant and FRC (ARF Grant No. R-144-000-278-112) for the financial support. We also acknowledge the funding support from the Singapore NRF through the Singapore-Berkeley Research Initiative for Sustainable Energy (SinBeRISE) CREATE Programme. Sinu Mathew would like to acknowledge support from the Grant R-398-000-070-133. We also acknowledge the support from NRF and MOE Singapore Grants NRF-CRP 8-2011-06 and MOE-AcRFTier-2 (MOE2010-T2-2-121). Xiao Renshaw Wang would like to thank the support from NWO Rubicon Grant (2011, 680-50-1114). We thank Prof. J. M. D. Coey (Trinity College, Dublin) for fruitful discussions. We acknowledge Mr. Amar Srivastava and Dr. Surajit Saha for the XRD measurement and analysis. Sinu Mathew would also like to acknowledge Mr. Shawn Lee Ken Seng (WITec, Singapore) for the Raman microscopy experiments.

Supporting Information Available: The details of PLD growth of LaAlO₃/SrTiO₃ sample along with RHEED analysis and a table of various samples characterized. Electrical transport data of ion-irradiated low carrier density ($n_s = 3 \times 10^{13} \text{ cm}^{-2}$) sample. Raman spectroscopy data of the ion-irradiated SrTiO₃. Details of spectroscopic ellipsometry data analysis. HRRBS spectrum and analysis. Electrical and magnetotransport study of the 500 keV helium ion-irradiated LaAlO₃/SrTiO₃ sample. This material is available free of charge via the Internet at <http://pubs.acs.org>.

REFERENCES AND NOTES

- Ohtomo, A.; Hwang, H. Y. A High-Mobility Electron Gas at the LaAlO₃/SrTiO₃ Heterointerface. *Nature* **2004**, *427*, 423–426.
- Reyren, N.; Thiel, S.; Caviglia, A. D.; Fitting Kourkoutis, L.; Hammerl, G.; Richter, C.; Schneider, C. W.; Kopp, T.; Ruetschi, A. S.; Jaccard, D.; *et al.* Superconducting Interfaces between Insulating Oxides. *Science* **2007**, *317*, 1196–1199.
- Brinkman, A.; Huijben, M.; Van Zalk, M.; Huijben, J.; Zeitler, U.; Maan, J. C.; van der Wiel, W. G.; Rijnders, G.; Blank, D. H. A.; Hilgenkamp, H. Magnetic Effects at the Interface between Non-Magnetic Oxides. *Nat. Mater.* **2007**, *6*, 493–496.
- Ariando; Wang, X.; Baskaran, G.; Liu, Z. Q.; Huijben, J.; Yi, J. B.; Annadi, A.; Roy Barman, A.; Ruydy, A.; Feng, Y. P.; *et al.* Electronic Phase Separation at the LaAlO₃/SrTiO₃ Interface. *Nat. Commun.* **2011**, *2*, 188.
- Bert, J. A.; Kalisky, B.; Bell, C.; Kim, M.; Hikita, Y.; Hwang, H. Y. Direct Imaging of the Coexistence of Ferromagnetism and Superconductivity at the LaAlO₃/SrTiO₃ Interface. *Nat. Phys.* **2011**, *7*, 767–771.
- Lu, Li; Richter, C.; Mannhart, J.; Ashoori, R. C. Coexistence of Magnetic Order and Two-Dimensional Superconductivity at LaAlO₃/SrTiO₃ Interfaces. *Nat. Phys.* **2011**, *7*, 762–766.
- Thiel, S.; Hammerl, G.; Schmehl, A.; Schneider, C. W.; Mannhart, J. Tunable Quasi-Two-Dimensional Electron Gases in Oxide Heterostructures. *Science* **2006**, *313*, 1942–1945.
- Cen, C.; Thiel, S.; Hammerl, G.; Schneider, C. W.; Andersen, K. E.; Hellberg, C. S.; Mannhart, J.; Levy, J. Nanoscale Control of an Interfacial Metal–Insulator Transition at Room Temperature. *Nat. Mater.* **2008**, *7*, 298–302.
- Caviglia, A. D.; Gabay, M.; Gariglio, S.; Reyren, N.; Cancellieri, C.; Triscone, J.-M. Tunable Rashba Spin-Orbit Interaction at Oxide Interfaces. *Phys. Rev. Lett.* **2010**, *104*, 126803.
- Ben Shalom, M.; Sachs, M.; Rakhmilevitch, D.; Palevski, A.; Dagan, Y. Tuning Spin-Orbit Coupling and Superconductivity at the SrTiO₃/LaAlO₃ Interface: A Magnetotransport Study. *Phys. Rev. Lett.* **2010**, *104*, 126802.
- Annadi, A.; Zhang, Q.; Wang, X.; Tuzla, N.; Gopinadhan, K.; Lu, W. M.; Barman, Roy.; Liu, Z. Q.; Srivastava, A.; Saha, S.; *et al.* Anisotropic Two-Dimensional Electron Gas at the LaAlO₃/SrTiO₃ (110) Interface. *Nat. Commun.* **2013**, *4*, 1838.
- Fidkowski, L.; Jiang, H. C.; Lutchny, R. M.; Nayak, C. Magnetic and Superconducting Ordering in One-Dimensional Nanostructures at the LaAlO₃/SrTiO₃ Interface. *Phys. Rev. B: Condens. Matter Mater. Phys.* **2013**, *87*, 014436.
- Irvin, P.; Ma, Y.; Bogorin, D. F.; Cen, Cheng.; Bark, C. W.; Folkman, C. M.; Eom, C. B.; Levy, J. Rewritable Nanoscale Oxide Photodetector. *Nat. Photonics* **2010**, *4*, 849–852.
- Tebano, A.; Fabbri, E.; Pergolesi, D.; Balestrino, G.; Traversa, E. Room-Temperature Giant Persistent Photoconductivity in SrTiO₃/LaAlO₃ Heterostructures. *ACS Nano* **2012**, *6*, 1278–1283.
- Cheng, G.; Veazey, J. P.; Irvin, P.; Cen, C.; Bogorin, D. F.; Bi, F.; Huang, M.; Lu, S.; Bark, C. W.; Ryu, S.; Cho, K. H.; *et al.* Anomalous Transport in Sketched Nanostructures at the LaAlO₃/SrTiO₃ Interface. *Phys. Rev. X* **2013**, *3*, 011021.
- Schneider, C. W.; Thiel, S.; Hammerl, G.; Richter, C.; Mannhart, J. Microlithography of Electron Gases Formed at Interfaces in Oxide Heterostructures. *Appl. Phys. Lett.* **2006**, *89*, 122101.
- Banerjee, N.; Huijben, M.; Koster, G.; Rijnders, G. Direct Patterning of Functional Interfaces in Oxide Heterostructures. *Appl. Phys. Lett.* **2012**, *100*, 041601.
- Foerster, M.; Bachelet, R.; Laukhin, V.; Fontcuberta, J.; Herranz, G.; Sánchez, F. Laterally Confined Two-Dimensional Electron Gases in Self-Patterned LaAlO₃/SrTiO₃ Interfaces. *Appl. Phys. Lett.* **2012**, *100*, 231607.
- Kan, D.; Terashima, T.; Kanda, R.; Masuno, A.; Tanaka, K.; Chu, S.; Kan, H.; Ishizumi, A.; Kanemitsu, Y.; Shimakawa, Y.; Takano, M. Blue-Light Emission at Room Temperature from Ar⁺-Irradiated SrTiO₃. *Nat. Mater.* **2005**, *4*, 816–819.
- Krasheninnikov, A. V.; Banhart, F. Engineering of Nanostructured Carbon Materials with Electron or Ion Beams. *Nat. Mater.* **2007**, *6*, 723–733.
- Krasheninnikov, A. V.; Nordlund, K. Ion and Electron Irradiation-Induced Effects in Nanostructured Materials. *J. Appl. Phys.* **2010**, *107*, 07130.
- Mathew, S.; Chan, T. K.; Gopinadhan, K.; Yu, X. J.; Zhan, D.; Cao, L.; Ruydy, A.; Breese, M. B. H.; Dhar, S.; Shen, Z. X.; *et al.* Magnetism in MoS₂ Induced by Proton Irradiation. *Appl. Phys. Lett.* **2012**, *101*, 102103.
- Mathew, S.; Satpati, B.; Joseph, B.; Dev, B. N.; Nirmala, R.; Malik, S. K.; Kesavamoorthy, R. Magnetism in C₆₀ Films Induced by 2 MeV Proton Irradiation. *Phys. Rev. B: Condens. Matter Mater. Phys.* **2007**, *75*, 75426.
- Wei, D.; Xie, L.; Lee, K. K.; Hu, Z.; Tan, S.; Chen, W.; Sow, C. H.; Chen, K.; Liu, Y.; Wee, A. T. S. Controllable Unzipping for Intramolecular Junctions of Graphene Nanoribbons and Single-Walled Carbon Nanotubes. *Nat. Commun.* **2013**, *4*, 1374.
- Gelfand, M. P.; Bradley, R. M. Highly Ordered Nanoscale Patterns Produced by Masked Ion Bombardment of a Moving Solid Surface. *Phys. Rev. B: Condens. Matter Mater. Phys.* **2012**, *86*, 121406(R).
- Russo, C. J.; Golovchenko, J. A. Atom-by-Atom Nucleation and Growth of Graphene Nanopores. *Proc. Natl. Acad. Sci. U. S. A.* **2012**, *109*, 5953–5957.
- Wolf, T.; Bergeal, N.; Lesueur, J.; Fourie, C. J.; Faini, G.; Ulysse, C.; Febvre, P. YBCO Josephson Junctions and Striplines for RSFQ Circuits Made by Ion Irradiation. *IEEE Trans. Appl. Supercond.* **2013**, *23*, 1101205.
- Watt, F.; Breese, M. B. H.; Bettiol, A. A.; Van Kan, J. A. Proton Beam Writing. *Mater. Today* **2007**, *10*, 20–29.
- Van Kan, J.; Bettiol, A. A.; Watt, F. Three-Dimensional Nanolithography Using Proton Beam Writing. *Appl. Phys. Lett.* **2003**, *83*, 1629–1631.
- Liang, H. D.; Kumar, V. S.; Wu, J. F.; Breese, M. B. H. Ion Beam Irradiation Induced Fabrication of Vertical Coupling Waveguides. *Appl. Phys. Lett.* **2013**, *102*, 131112.
- Kim, S.; Lee, S.; Jung, K.; Jangyup, S.; Minseok, K.; Shinill, K.; Hong, J. Nanoscale Patterning of Complex Magnetic

- Nanostructures by Reduction with Low-Energy Protons. *Nat. Nanotechnol.* **2012**, *7*, 567–571.
32. Hong, W.-K.; Jo, G.; Sohn, J. I.; Park, W.; Choe, M.; Wang, G.; Kahng, Ho Y.; Welland, M. E.; Lee, T. Tuning of the Electronic Characteristics of ZnO Nanowire Field Effect Transistors by Proton Irradiation. *ACS Nano* **2010**, *4*, 811–818.
 33. Bell, C.; Harashima, S.; Hikita, Y.; Hwang, H. Y. Thickness Dependence of the Mobility at the LaAlO₃/SrTiO₃ Interface. *Appl. Phys. Lett.* **2009**, *94*, 222111.
 34. Annadi, A.; Huang, Z.; Gopinadhan, K.; Wang, X. R.; Srivastava, A.; Liu, Z. Q.; Harsan Ma, H.; Sarkar, T. P.; Venkatesan, T.; *et al.* Fourfold oscillation in Anisotropic Magneto Resistance and Planar Hall Effect at the LaAlO₃/SrTiO₃ Heterointerfaces: Effect of Carrier Confinement and Electric Field on Magnetic Interactions. *Phys. Rev. B: Condens. Matter Mater. Phys.* **2013**, *87*, 201102(R).
 35. Annadi, A.; Putra, A.; Srivastava, A.; Wang, X.; Huang, Z.; Liu, Z. Q.; Venkatesan, T.; Ariando Evolution of Variable Range Hopping in Strongly Localized Two Dimensional Electron Gas at NdAlO₃/SrTiO₃ (100) Heterointerfaces. *Appl. Phys. Lett.* **2012**, *101*, 231604.
 36. Salluzzo, M.; Cezar, J. C.; Brookes, N. B.; Bisogni, V.; De Luca, G. M.; Richter, C.; Thiel, S.; Mannhart, J.; Huijben, M.; Brinkman, A.; *et al.* Orbital Reconstruction and the Two-Dimensional Electron Gas at the LaAlO₃/SrTiO₃ Interface. *Phys. Rev. Lett.* **2009**, *102*, 166804.
 37. Jang, H. W.; Felker, D. A.; Bark, C. W.; Wang, Y.; Niranjani, M. K.; Nelson, C. T.; Zhang, Y.; Su, D.; Folkman, C. M.; Baek, S. H.; *et al.* Metallic and Insulating Oxide Interfaces Controlled by Electronic Correlations. *Science* **2011**, *331*, 886–889.
 38. Annadi, A.; Putra, A.; Liu, Z. Q.; Wang, X.; Gopinadhan, K.; Huang, Z.; Dhar, S.; Venkatesan, T.; Ariando Electronic Correlation and Strain Effects at the Interfaces between Polar and Non-Polar Complex Oxides. *Phys. Rev. B: Condens. Matter Mater. Phys.* **2012**, *86*, 085450.
 39. Schoofs, F.; Egilmez, M.; Fix, T.; MacManus-Driscoll, J. L.; Blamire, M. G. Impact of Structural Transitions on Electron Transport at LaAlO₃/SrTiO₃ Heterointerfaces. *Appl. Phys. Lett.* **2012**, *100*, 081601.
 40. Schoofs, F.; Carpenter, M. A.; Vickers, M. E.; Egilmez, M.; Fix, T.; Kleibeuker, J. E.; MacManus-Driscoll, J. L.; Blamire, M. G. Carrier Density Modulation by Structural Distortions at Modified LaAlO₃/SrTiO₃ Interfaces. *J. Phys.: Condens. Matter* **2013**, *25*, 175005.
 41. Chen, Y.; Pryds, N.; Kleibeuker, J. E.; Koster, G.; Sun, J.; Stamate, E.; Shen, B.; Rijnders, G.; Linderoth, S. Metallic and Insulating Interfaces of Amorphous SrTiO₃-Based Oxide Heterostructures. *Nano Lett.* **2011**, *11*, 3774–3778.
 42. Cowley, R. A. Lattice Dynamics and Phase Transitions of Strontium Titanate. *Phys. Rev.* **1964**, *134*, A981–A997.
 43. Nilsen, W. G.; Skinner, J. G. Raman Spectrum of Strontium Titanate. *J. Chem. Phys.* **1968**, *48*, 2240–2248.
 44. Tenne, D. A.; Xi, X. Raman Spectroscopy of Ferroelectric Thin Films and Superlattices. *J. Am. Ceram. Soc.* **2008**, *91*, 1820–1834.
 45. Yuzyuk, Y. I. Raman Scattering Spectra of Ceramics, Films, and Superlattices of Ferroelectric Perovskites: A Review. *Phys. Solid State* **2012**, *54*, 026–1059.
 46. Sirenko, A. A.; Akimov, I. A.; Fox, J. R.; Clark, A. M.; Li, H.-C.; Si, W.; Xi, X. X. Observation of the First-Order Raman Scattering in SrTiO₃ Thin Films. *Phys. Rev. Lett.* **1999**, *82*, 4500–4503.
 47. Sarbajit, B.; Kim, Dae-In.; Robinson, D. R.; Irving, P. H.; Mao, Y.; Wong, S. S. Observation of Fano Asymmetry in Raman Spectra of SrTiO₃ and Ca_{1-x}Sr_xTiO₃ Perovskite Nanocubes. *Appl. Phys. Lett.* **2006**, *89*, 223130.
 48. Wu, X. W.; Wu, D. J.; Liu, X. J. Negative Pressure Effects in SrTiO₃ Nanoparticles Investigated by Raman Spectroscopy. *Soild State Commun.* **2008**, *145*, 255–258.
 49. Fleury, P. A.; Worlock, J. M. Electric-Field-Induced Raman Scattering in SrTiO₃ and KTaO₃. *Phys. Rev.* **1968**, *174*, 613–623.
 50. Cardona, M. Optical Properties and Band Structure of SrTiO₃ and BaTiO₃. *Phys. Rev.* **1965**, *140*, A651.
 51. Van Benthem, K.; Elsässer, C.; French, R. H. Bulk Electronic Structure of SrTiO₃: Experiment and Theory. *J. Appl. Phys.* **2001**, *90*, 6156.
 52. Sponza, L.; Vèniard, V.; Sottile, F.; Giorgetti, C.; Reining, L. Role of Localized Electrons in Electron-Hole Interaction: The Case of SrTiO₃. *Phys. Rev. B: Condens. Matter Mater. Phys.* **2013**, *87*, 235102.
 53. Zollner, S.; Demkov, A. A.; Liu, R.; Fejes, P. L.; Gregory, R. B. Optical Properties of Bulk and Thin-Film SrTiO₃ on Si and Pt. *J. Vac. Sci. Technol., B: Microelectron. Nanometer Struct.—Process., Meas., Phenom.* **2000**, *18*, 2242.
 54. Wang, S. Generalization of the Thomas-Reiche-Kuhn and the Bethe Sum Rules. *Phys. Rev. A: At., Mol., Opt. Phys.* **1999**, *60*, 262.
 55. Rusydi, A.; Rauer, R.; Neuber, G.; Bastjan, M.; Mahns, I.; Müller, S.; Saichu, P.; Schulz, B.; Singer, S. G.; Lichtenstein, A. I.; *et al.* M. Metal-Insulator Transition in Manganites: Changes in Optical Conductivity up to 22 eV. *Phys. Rev. B: Condens. Matter Mater. Phys.* **2008**, *78*, 125110.
 56. Ziegler, J. F.; Biersack, J. P.; Littmark, U. *The Stopping and Range of Ions in Matter*; Pergamon Press: New York, 1995.